

OPTICS

Photo-induced cascaded harmonic and comb generation in silicon nitride microresonators

Jianqi Hu^{1†}, Edgars Nitiss^{1†}, Jijun He², Junqiu Liu², Ozan Yakar¹, Wenle Weng^{2‡}, Tobias J. Kippenberg², Camille-Sophie Brès^{1*}

Silicon nitride (Si_3N_4) is an ever-maturing integrated platform for nonlinear optics but mostly considered for third-order [$\chi^{(3)}$] nonlinear interactions. Recently, second-order [$\chi^{(2)}$] nonlinearity was introduced into Si_3N_4 via the photogalvanic effect, resulting in the inscription of quasi-phase-matched $\chi^{(2)}$ gratings. However, the full potential of the photogalvanic effect in microresonators remains largely unexplored for cascaded effects. Here, we report combined $\chi^{(2)}$ and $\chi^{(3)}$ nonlinear effects in a normal dispersion Si_3N_4 microresonator. We demonstrate that the photo-induced $\chi^{(2)}$ grating also provides phase-matching for the sum-frequency generation process, enabling the initiation and successive switching of primary combs. In addition, the doubly resonant pump and second-harmonic fields allow for effective third-harmonic generation, where a secondary optically written $\chi^{(2)}$ grating is identified. Last, we reach a broadband microcomb state evolved from the sum-frequency-coupled primary comb. These results expand the scope of cascaded effects in microresonators.

INTRODUCTION

Optical microresonators made of low-loss and highly nonlinear materials have emerged as prominent systems for the observation and the understanding of the rich landscape of nonlinear physics. Typical nonlinear interactions in microresonators encompass second-order [$\chi^{(2)}$] (1) and third-order [$\chi^{(3)}$] (2) parametric processes, as well as photon-phonon processes, such as Raman (3) and Brillouin (4) scatterings. Specifically, $\chi^{(3)}$ nonlinearity is ubiquitous in all material platforms and thus mostly exploited, enabling third-harmonic (TH) generation (5) or Kerr frequency comb generation (6). The past decades have witnessed extensive microcomb studies, evolving rapidly from the primary combs (7) to broadband, mode-locked states where dissipative Kerr solitons (8) or dark pulses (9) are formed. This has subsequently found numerous applications thanks to the mutually coherent and massively parallel microcomb lines (10).

Unlike the widely accessible Kerr effect in microresonators, $\chi^{(2)}$ nonlinearity is only intrinsic to noncentrosymmetric media. Notably, $\chi^{(2)}$ response is essential for electro-optic effect and underpins various three-wave mixing parametric processes, for example, second-harmonic (SH) generation (11–16). Efficient SH has been generated in $\chi^{(2)}$ microresonators in lithium niobate (11–13) and III-V materials (14–16). Beyond SH generation, cascaded $\chi^{(2)}$ processes resulting in comb formation have been observed (17, 18), as $\chi^{(2)}$ cavities also display effective $\chi^{(3)}$ nonlinearity (19–21). In addition, parametrically driving $\chi^{(2)}$ microresonators could allow for the onset of optical parametric oscillation (22–25). This has further led to the recent observation of quadratic solitons in $\chi^{(2)}$ microresonators (26) akin to localized structures in $\chi^{(3)}$ microresonators (10).

However, with the exception of silicon carbide (27, 28), conventional silicon photonic materials [e.g., silicon, silica, and silicon nitride (Si_3N_4)] lack intrinsic $\chi^{(2)}$ response. To bring $\chi^{(2)}$ into these complementary metal-oxide semiconductor-compatible materials, diverse approaches have been pursued (29–37). Paradigm demonstrations include symmetry breaking in silicon waveguides induced by applied electric fields (29, 30) or via charged defects (31) and all-optical poling of Si_3N_4 waveguides based on the photogalvanic effect (32–36). With regard to resonator structures, effective $\chi^{(2)}$ can also be optically induced in Si_3N_4 microresonators manifesting in efficient SH generation (38–40).

SH generation in microresonators without periodically poled (12, 13) or crystallographic (15) quasi-phase-matching (QPM) structures had long been achieved by intermodal phase matching between involved fundamental-harmonic (FH; i.e., pump) and SH resonances. Opposed to this convention, we have recently observed in Si_3N_4 that periodic space charges are self-organized along the circumferences of microresonators when the pump and its SH are doubly resonant (40). The alternating electric field, together with the $\chi^{(3)}$ nonlinearity of Si_3N_4 , results in an effective $\chi^{(2)}$ grating (41–43), with a periodicity following the interference of FH and SH and thus automatically compensating their phase mismatch. Such fully adaptive QPM greatly eases the efforts for meeting phase-matching condition, posing Si_3N_4 microresonators as ideal test beds to investigate various $\chi^{(2)}$ nonlinear effects beyond SH generation. Meanwhile, Si_3N_4 is indisputably one of the most popular platforms for Kerr microcomb research (9, 44–47).

The combined $\chi^{(2)}$ and $\chi^{(3)}$ combs have indeed been observed in Si_3N_4 microresonators (48, 49), albeit the presence of $\chi^{(2)}$ being attributed to intermodal phase matching. Now, with the better understanding of $\chi^{(2)}$ phase-matching mechanism in Si_3N_4 microresonators (40), it is worth coming back to these cascaded nonlinear effects. In addition, we have recently generalized the photogalvanic effect to nondegenerate arbitrary three-wave condition, whose interference could inscribe the required QPM for the corresponding sum-frequency (SF) conversion process (36). This can be beneficial, for instance, in frequency tripling through cascaded SF

¹École Polytechnique Fédérale de Lausanne, Photonic Systems Laboratory (PHOSL), STI-HEM, Station 11, Lausanne CH-1015, Switzerland. ²École Polytechnique Fédérale de Lausanne, Laboratory of Photonics and Quantum Measurements (LPQM), SB-IPHYS, Station 3, Lausanne CH-1015, Switzerland.

[†]These authors contributed equally to the work.

[‡]Present address: Institute for Photonics and Advanced Sensing (IPAS) and School of Physical Sciences, The University of Adelaide, Adelaide, South Australia 5005, Australia.

*Corresponding author. Email: camille.bres@epfl.ch

generation, which is now a standard and commercially available technology to generate TH light (50). Although frequency tripling has been experimentally shown in Si_3N_4 waveguides (36), the responsible SF grating is rather weak, and its full potential in resonator structures remains unexplored.

Here, we demonstrate versatile $\chi^{(2)}$ and $\chi^{(3)}$ nonlinear effects in a high-quality factor (Q), normal dispersion Si_3N_4 microresonator. A tunable continuous-wave (CW) laser is injected into the fundamental pump resonances of the microresonator. By varying the pump detuning, the doubly resonant condition of the pump mode and one of the several SH modes are easily matched, thanks to the small free spectral range (FSR; ~ 25 GHz) and multimode nature of the microresonator used. This gives rise to the photo-induced $\chi^{(2)}$ grating inside the microresonator enabling QPM for SH generation (40). Following the FH-SH grating inscription, we show here that the combined $\chi^{(2)}$ and $\chi^{(3)}$ nonlinearities can lead to the cascaded nonlinear processes, such as the generation of cascaded harmonic and frequency combs. In our system, the cascaded harmonic generation, which produces effective TH light, is a $\chi^{(2)}$ process resulting from the photogalvanic effect, based on the coherent interference among the FH, the generated SH, and the seed effective TH waves. We confirm this using two-photon microscopy (TPM) imaging of the poled microresonator (34, 35, 40), where a secondary $\chi^{(2)}$ grating responsible for the QPM of the underlying FH-SH-TH process is clearly identified. In addition, we observe the generation of primary combs in the FH band together with SF generation in the SH band. The first-order comb sideband and the SF component are efficiently coupled through the SF generation process and can be successively switched while tuning the pump further into the resonance. Here, the phase matching of the SF generation process is the same as the SH generation, thereby guaranteed by the already inscribed FH-SH grating. Besides, the SF-coupled primary comb also facilitates the excitation of localized states in the normal dispersion regime (51). As a consequence, a low-noise and broadband microcomb featuring typical spectral envelope of a dark pulse is deterministically reached in the experiment. Our work reports various cascaded nonlinear phenomena in an optically poled Si_3N_4 microresonator and is potentially applicable for f -2f or $2f$ -3f comb self-referencing (52, 53).

RESULTS

$\chi^{(2)}$ and $\chi^{(3)}$ nonlinear processes in Si_3N_4 microresonators

In this study, we use a large radius, normal dispersion Si_3N_4 microresonator (see Materials and Methods) with no notable mode crossings in the pump spectral region (see note S1). Kerr comb generation in such microresonators is considered difficult with typical CW driving (54), as combs in normal dispersion regime are generally initiated by leveraging perturbations from spatial mode coupling (55, 56) or self-injection locking (57). However, in this work, we show that multiple nonlinear processes can be enabled by the photogalvanic effect, resulting in harmonic generation and comb generation. Figure 1A illustrates the energy and momentum conservation diagrams of these processes. In the experiment, a CW pump at angular frequency ω is slowly scanned by decreasing its frequency to stably access a pump resonance. While sweeping, if a certain SH mode resonance matches the frequency 2ω , then the microresonator becomes doubly resonant, and the photogalvanic effect could occur (39, 40). The phase matching is automatically

realized via a self-organized $\chi^{(2)}$ grating, inscribed following the interference of resonating FH and initially very weak SH. We can rewrite the phase mismatch as $\Delta k_1 = k_{2\omega} - 2k_\omega = (m_{2\omega} - 2m_\omega)/R$ (40) with m_ω and $m_{2\omega}$ as the azimuthal mode numbers of FH and SH resonances, respectively, and R as the radius of the microresonator. The corresponding QPM condition is given by $|\Delta k_1| = 2\pi/\Lambda_1$ with Λ_1 the grating period. Hence, the grating period length is derived as $\Lambda_1 = 2\pi R / |m_{2\omega} - 2m_\omega|$, and the total number of grating periods per perimeter writes $N_1 = |m_{2\omega} - 2m_\omega|$. As depicted by the artistic representation in Fig. 1B (top), the $\chi^{(2)}$ QPM grating in turn drastically amplifies the process, leading to efficient SH generation.

After the inscription of the FH-SH grating for SH generation, a series of cascaded nonlinear processes follow when the pump frequency is further scanned within the resonance. These include SF generation, comb generation, and cascaded harmonic generation as detailed in Fig. 1A. The SF and primary comb generation is explained in Fig. 1C, where the relative distributions of FH and SH resonances at different pump detunings are shown. Initially, the doubly resonant condition is fulfilled so that frequency 2ω is generated (region I). Here, the FSRs of different SH modes are smaller than the pump resonance FSR (see note S1), and SH resonances redshift faster than the pump resonance while detuning (40). As a consequence, the SH resonance gradually walks off during pump detuning, while the resonance frequency matching among the FH mode at ω , FH sideband mode at $\omega - \Delta\omega$, and SF mode at $2\omega - \Delta\omega$, with $\Delta\omega$ approximately the FSR at pump, can be realized (region II). It is important to note that such a three-wave process is also phase-matched, given that the azimuthal mode number mismatch among three waves is the same as the number of inscribed grating periods in SH generation, i.e., $|(m_{2\omega} - 1) - m_\omega - (m_\omega - 1)| = N_1$. The nonlinear coupling via the SF process modifies locally the phase of this particular sideband mode, enabling degenerate four-wave mixing (FWM) even in the normal dispersion regime and simultaneous SF generation (49). If further pump detuning is possible, then the SF coupled mode at FH will be successively downshifted to $\omega - n\Delta\omega$, leading to primary comb generation with comb FSR of $n\Delta\omega$ and SF generation at a frequency of $2\omega - n\Delta\omega$ (region III, $n = 2$ is shown). Flexible primary comb FSR switching can thereby be obtained in a single pump resonance via the dynamic coupling. This is in contrast to the conventional spatial mode-induced coupling (55, 56), where the crossing position is generally fixed so that the comb FSR is varied by pumping different resonances. We also theoretically analyze the modulational instability (MI) of the process based on coupled Lugiato-Lefever equations (see note S2) (21, 49, 58). Net gain is indeed observed in simulation with the peak position increasing with the pump detuning, confirming the phenomenon depicted in Fig. 1C.

The cascaded harmonic generation also takes place in the microresonator given the presence of the SH field, leading to effective TH light generation. Here, the TH is induced by the nondegenerate photogalvanic effect based on the cascaded SF generation from FH and SH waves, unlike an intermodal phase-matched $\chi^{(3)}$ TH generation process (5, 59) but similar to a typical $\chi^{(2)}$ SF process in frequency tripling (50). To distinguish the process from the abovementioned SF generation relying on the same $\chi^{(2)}$ QPM grating for SH generation, we term the process here as cascaded harmonic generation or effective TH generation interchangeably to avoid ambiguity. Reference (36) has highlighted that three arbitrary

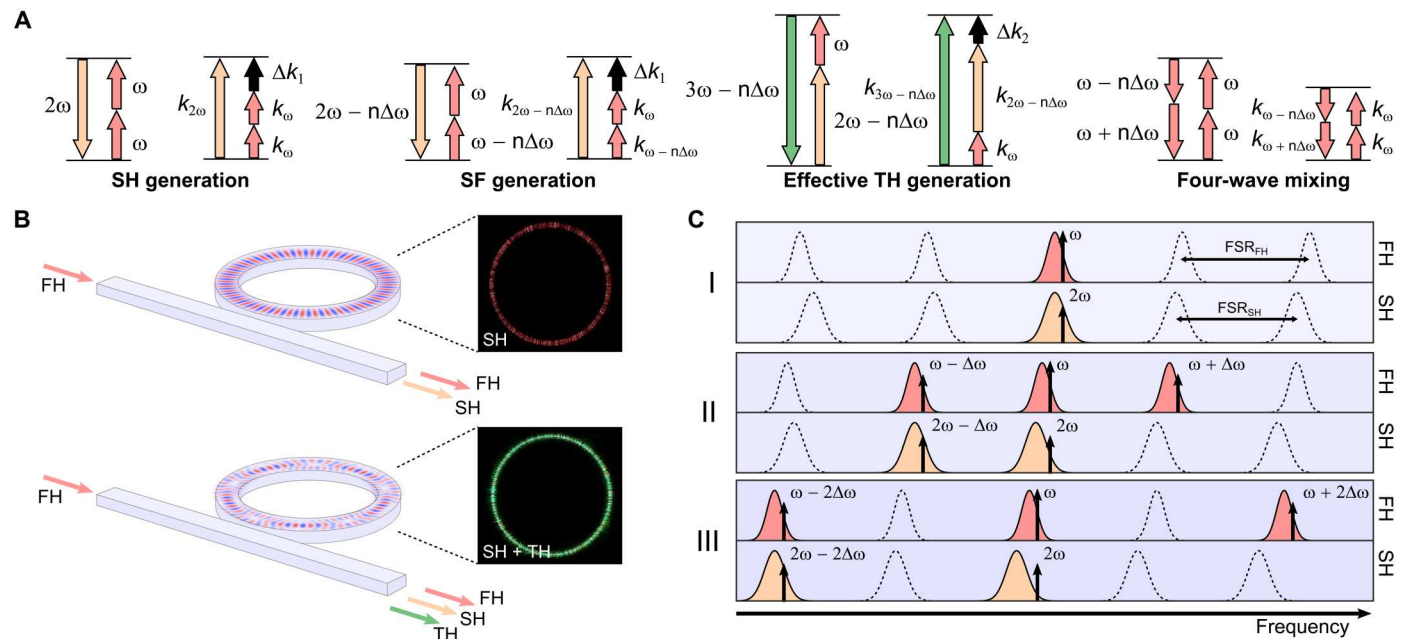


Fig. 1. Photogalvanic effect enabled processes in Si_3N_4 microresonators. (A) Illustration of energy and momentum conservation of the available processes inside the device: SH generation, SF generation, effective TH generation, and FWM. SH, SF, and effective TH generation processes are present due to QPM of participating waves enabled by the photogalvanic effect. FWM process is initiated with the assistance of SF coupling. (B) Artistic representation of $\chi^{(2)}$ QPM grating structures optically inscribed in the Si_3N_4 microresonator. The top part illustrates the FH-SH grating inscription when SH is generated, while the bottom part illustrates the inscription of superimposed FH-SH and FH-SH-TH gratings when SH and effective TH are both generated. Optical microscope images of the scattered light from the microresonator are shown for both cases. (C) Relative resonance distribution at FH and SH bands in SF-coupled FWM process. By tuning the pump frequency ω into the resonance (decreasing ω), the SH resonances red-shift faster than the FH resonances. During the detuning, the doubly resonant condition for pump ω and its SH 2ω is met, leading to $\chi^{(2)}$ grating inscription and SH generation (I). When the pump is further detuned, the frequency matching of the SF process among modes ω , $\omega - \Delta\omega$, and $2\omega - \Delta\omega$ is achieved, while its phase matching is guaranteed by the already inscribed $\chi^{(2)}$ grating. The SF-coupled FWM occurs manifested by the simultaneous generation of sideband modes $\omega \pm \Delta\omega$ at FH and SF mode $2\omega - \Delta\omega$ at SH (II). The coupled SF mode can be successively downshifted, and the FSR of the FH comb is varied accordingly (III).

coherent waves that are frequency matched could yield a periodic electric field to compensate for their unmatched momenta. Hence, as shown in Fig. 1A, the SH and effective TH waves can also be offset at frequencies of $2\omega - n\Delta\omega$ and $3\omega - n\Delta\omega$, respectively. This offset depends on the resonant condition of the waves, as similar to SH generation, and the process now requires triply resonant to be initiated. Under such a circumstance, the interference of the three waves results in a self-organized FH-SH-TH grating due to the photogalvanic effect. Once again, the number of grating periods will exactly compensate the azimuthal mode number mismatch among three waves, in this case, given by $N_2 = |(m_{3\omega} - n) - (m_{2\omega} - n) - m_\omega| = |m_{3\omega} - m_{2\omega} - m_\omega|$ or equivalently the phase mismatch $\Delta k_2 = (m_{3\omega} - m_\omega - m_{2\omega})/R$. Therefore, there should be two superimposed periodic electric fields written in the microresonator that are respectively phase-matched for the FH-SH and FH-SH-TH processes, as illustrated by the artistic representation in Fig. 1B (bottom). The scheme is similar to frequency tripling achieved in a single $\chi^{(2)}$ crystal by optimizing the design of quasi-periodic domains (60), while our method automatically inscribes optimized QPM domains mediated by the photogalvanic effect.

$\chi^{(2)}$ grating imaging and analysis

The $\chi^{(2)}$ grating in the microresonator is inscribed by coupling a CW pump into resonances at C-band (see note S3). After such optical poling, we use TPM imaging technique to characterize the grating structure (34, 35, 40). The detail of TPM measurement and

the following image processing are described in Materials and Methods. In essence, the approach allows for the extraction of $\chi^{(2)}$ grating shapes along the circumference of microresonator and their spatial frequencies through spatially resolved Fourier analysis. This enables precise identification of the grating periods, which is essential for determining the modes interacting during the photogalvanic process.

Figure 2 showcases several processed $\chi^{(2)}$ grating images after the coordinate transformation (see Materials and Methods). All these diverse grating images are attained from the same microresonator but are written at three different pump resonances with different detuning conditions. Figure 2 (A to C) corresponds to the $\chi^{(2)}$ gratings inscribed when the pump is slightly tuned into resonances near 1544.40, 1547.35, and 1552.34 nm, respectively. Only SH is generated (see Fig. 1B, photo of the microresonator glowing red) in these cases, and no cascaded nonlinear effect is observed. The grating structure in the microresonator is given by the nonlinear interference of the involved FH and SH waves, i.e., $\chi^{(2)}(\phi) \sim \text{Re} \{ E_{2\omega} (E_\omega^*)^2 e^{i\Delta k_1 R \phi} \}$, where E_ω and $E_{2\omega}$ are the optical fields at FH and SH, respectively. $\text{Re} \{ \}$ is the real part of a complex number, and $*$ stands for the complex conjugate. In TPM images, the actual measured SH intensity is proportional to $[\chi^{(2)}(\phi)]^2$. The mode profiles and effective refractive indices of FH and several lower-order SH modes (SH1 to SH3) are extracted from the COMSOL Multiphysics simulation (see note S1). On the basis of

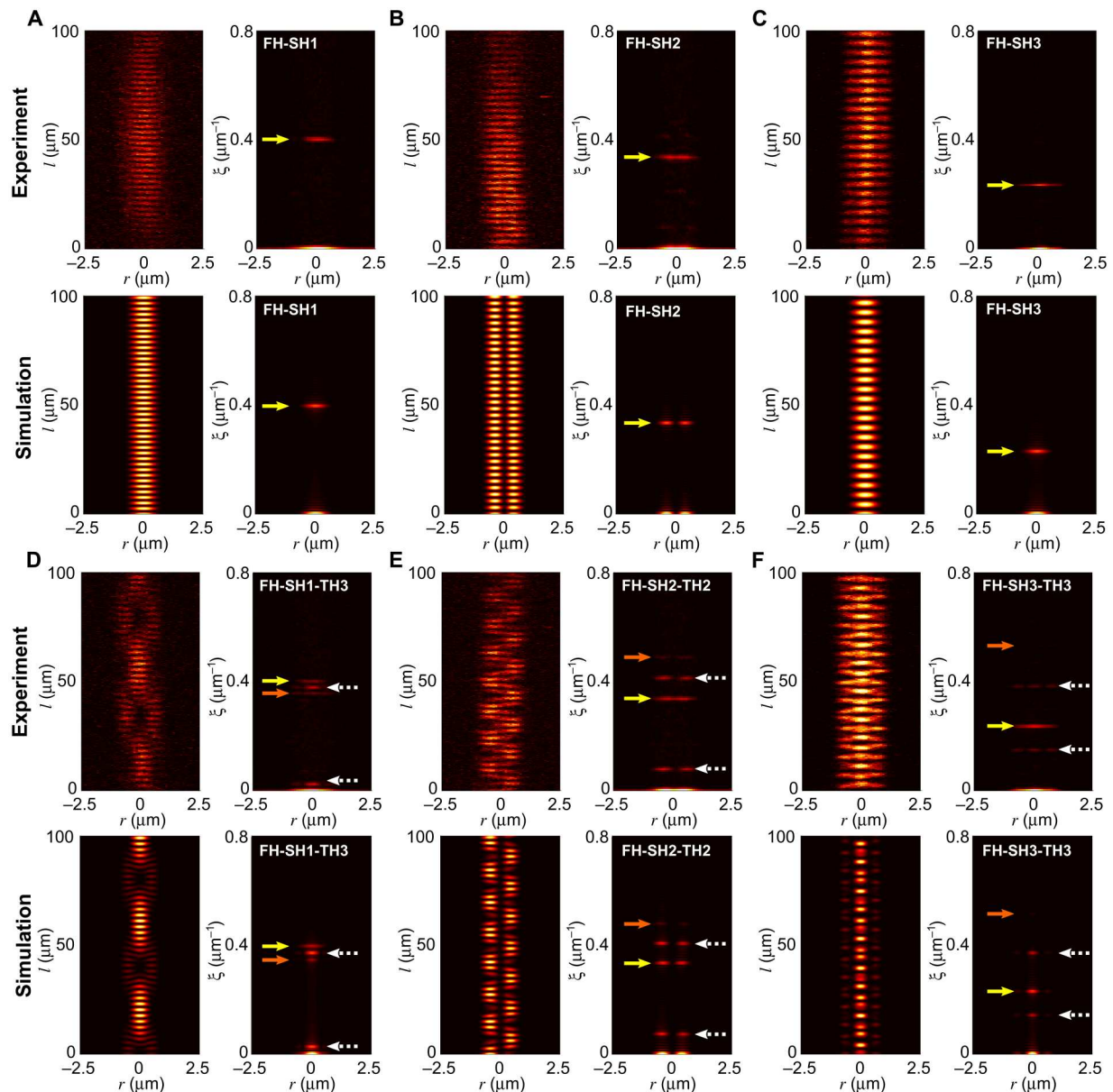


Fig. 2. Imaging and identification of inscribed $\chi^{(2)}$ gratings in the Si_3N_4 microresonator. (A to C) FH-SH grating structures (plotted along the circumference of the microresonator) and their spatial frequency graphs obtained by the Fourier transform. Top, experiment; bottom, simulation. The gratings in (A) to (C) are inscribed by slightly tuning the pump into the resonances near 1544.40, 1547.35, and 1552.34 nm, respectively. On the basis of the retrieved spatial frequencies (yellow arrows), the participating SH modes in the FH-SH photogalvanic process are identified as SH1, SH2, SH3, respectively. (D to F) Superimposed FH-SH and FH-SH-TH grating structures and their spatial frequency graphs. Top, experiment; bottom, simulation. The gratings in (D) to (F) are inscribed by further tuning the pump into the same resonances as in (A) to (C), respectively. Multiple Fourier components are observed corresponding to the spatial frequencies of the FH-SH gratings [yellow arrows, the same as in (A) to (C)], the FH-SH gratings (orange arrows), and the interference of the two gratings (white dashed arrows). In (D) to (F), the effective TH modes involved in the FH-SH-TH photogalvanic process are identified as TH3, TH2, and TH3, respectively.

these, we can simulate the corresponding grating patterns (40) and identify their participating SH modes in Fig. 2 (A to C) to be SH1, SH2, and SH3, respectively. The Fourier transform additionally confirms that there is only one dominant spatial frequency for each case ($2|\Delta k_1|$, indicated by the yellow arrow).

When the pump is further tuned into the same resonances near 1544.40, 1547.35, and 1552.34 nm, cascaded nonlinear effects including effective TH generation are observed while SH generation

is still maintained (see Fig. 1B, photo of the microresonator glowing green). To verify that the TH light results from the photogalvanic induced $\chi^{(2)}$ nonlinearity instead of intermodal $\chi^{(3)}$ process, we again image the poled microresonator generating TH using the TPM. Complex $\chi^{(2)}$ grating patterns of "chain," "zipper," and "necklace" shapes are captured and shown in Fig. 2 (D to F), respectively. From the Fourier transform, we can decompose the superimposed grating structures into their Fourier components, where multiple

spatial frequencies are now identified, in contrast to the single spatial frequency observed in Fig. 2 (A to C). Considering that the $\chi^{(2)}$ grating is composed of two parts separately phase-matched for FH-SH and FH-SH-TH generation processes, the $\chi^{(2)}$ response can be written as

$$\chi^{(2)}(\phi) \sim \text{Re} \{ E_{2\omega} (E_{\omega}^*)^2 e^{i\Delta k_1 R\phi} + a_0 E_{3\omega} E_{\omega}^* E_{2\omega}^* e^{i\Delta k_2 R\phi - i\phi_0} \},$$

where $E_{3\omega}$ is the resonant effective TH field, and a_0 and ϕ_0 are the relative amplitude and phase between the two gratings, respectively. We have assumed that the participating SH (TH) field here in the FH-SH-TH photogalvanic process is at frequency 2ω (3ω) as its mode profile and effective index barely change with a small offset n . We clearly see that the measured $\{\chi^{(2)}(\phi)\}^2$ responses have four nonzero spatial frequencies, i.e., $2|\Delta k_1|$, $2|\Delta k_2|$, $|\Delta k_1 + \Delta k_2|$, and $|\Delta k_1 - \Delta k_2|$. We note that one of the spatial frequencies in Fig. 2 (D to F), indicated again by the yellow arrow, is identical to the frequency extracted from Fig. 2 (A to C). This implies that the participating SH mode remains the same within each pump resonance while varying the pump detuning. Afterward, we identify in Fig. 2 (D to F) the spatial frequency of the secondary grating ($2|\Delta k_2|$; orange arrow) and the interference between the two gratings ($|\Delta k_1 + \Delta k_2|$, $|\Delta k_1 - \Delta k_2|$; white dashed arrows) according to their frequency relations. In case the secondary grating is weak, its spatial frequency can still be easily retrieved based on the interference components. From the extracted secondary frequency, we infer the involved effective TH mode in the photogalvanic process and then reconstruct the grating shape using simulated mode profiles (see note S1). By considering the involved effective TH modes

to be TH3, TH2, and TH3 in Fig. 2 (D to F), respectively, the simulated grating structures are reproduced very well as the measurement results both in terms of grating shapes and periods. In comparison, for the TH generation via $\chi^{(3)}$ nonlinearity requires the participation of a higher-order TH mode to achieve perfect phase matching (59).

Because of the minimal out-coupling of TH light from the microresonator, the conversion efficiency of effective TH generation here is in the same order of what has been measured in Si_3N_4 waveguides (36) but is much lower than poled lithium niobate microresonators (61). The efficiency can be improved significantly with proper chip design to maximally extract the generated effective TH. Nevertheless, the relatively low photo-induced $\chi^{(2)}$ in Si_3N_4 represents a fundamental limiting factor when very high efficiency is targeted for cascaded harmonic generation. Given the mismatch between simulation and fabrication, designing the exact triply resonant condition with desired mode interaction is practically challenging. The large waveguide cross section and the small FSR of the microresonator we used here are not optimal from the conversion efficiency point of view, but they facilitate the observation of cascaded harmonic generation, as it supports abundant spatial modes at harmonic bands and holds higher probability for being triply resonant. In addition, the resonant condition may be fine-tuned by leveraging thermo-optic control such that switching on and off the photogalvanic effect for the cascaded process.

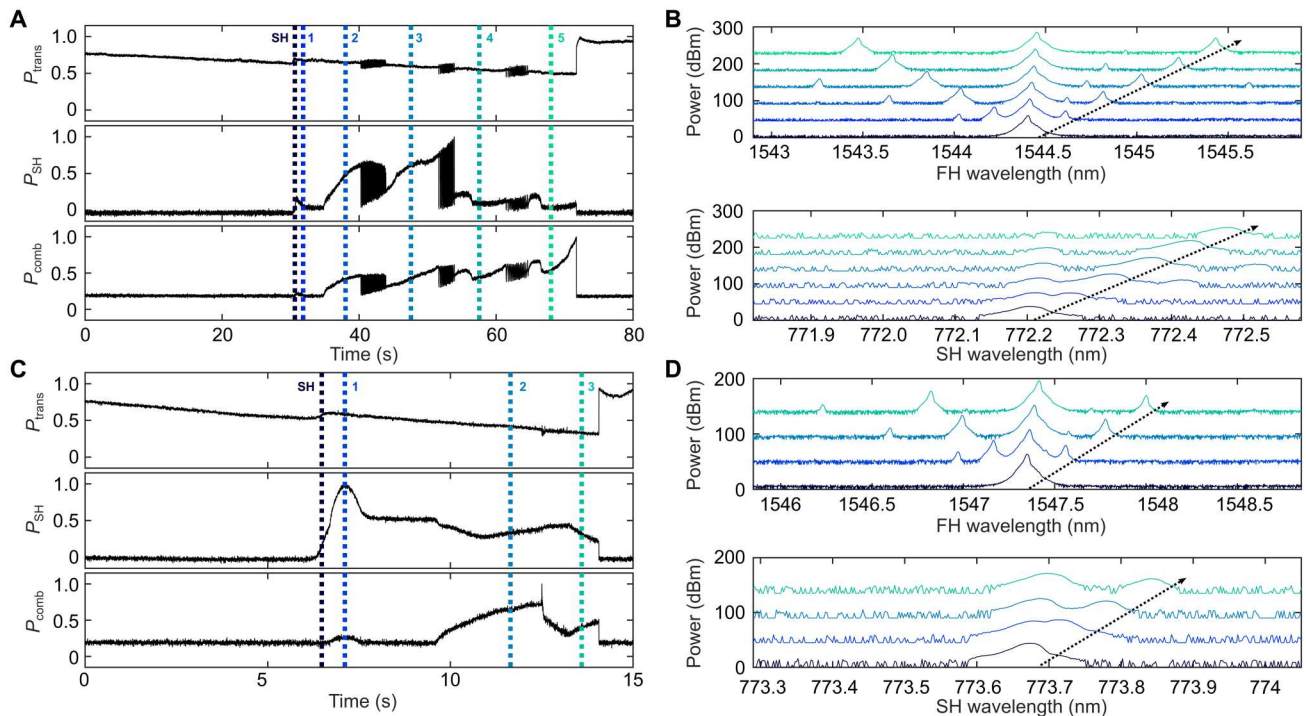


Fig. 3. Consecutive switching of the primary comb FSR and the SF mode. (A) Evolution of pump transmission (P_{trans}), generated SH power (P_{SH}), and comb power (P_{comb}) during the pump wavelength sweep across the resonance at 1544.40 nm. (B) The measured FH (top) and SH (bottom) spectra at the regions indicated by the vertical colored lines in (A). (C) Evolution of P_{trans} , P_{SH} , and P_{comb} during the pump wavelength sweep across the resonance at 1547.35 nm. (D) The FH (top) and SH (bottom) spectra at the regions indicated by the vertical colored lines in (C). For both resonances, after the inscription of $\chi^{(2)}$ gratings (SH generation), primary combs are initiated with the simultaneous generation of SF components. The FSR of the primary comb and the generated SF are then successively switched. The dashed lines in (B) and (D) denote the shifting of the coupled sideband modes at FH and SH bands.

Switchable primary comb and SF generation

The photo-induced $\chi^{(2)}$ gratings also allow for the primary comb and SF generation in the normal dispersion microresonator. To characterize them, we use an experimental setup that measures the transmission curves and the generated optical spectra at both pump and SH wavelengths (see note S3). When the pump frequency is slowly scanned across the 1544.40-nm resonance, the transmission curves of pump, SH, and comb power (P_{trans} , P_{SH} , and P_{comb} , respectively) are recorded and plotted in Fig. 3A. Figure 3B shows the measured FH and SH spectra at different pump detunings corresponding to the vertical dashed lines in Fig. 3A. These spectral plots are stacked and shifted in the y axis by 45 dB for clarity. From the transmission curves, we see that the primary comb generation at FH is initiated after SH generation. Further laser tuning into the resonance results in FSR switching of the primary combs from one to five FSR, in steps of one FSR (guided by the dashed arrow), before the pump exits its resonance. In the meantime, we can clearly observe the generation of the SF mode at the SH band, whose mode index is also downshifted by one to five FSR away from the SH mode (guided by the dashed arrow). In addition, we notice that the generated primary comb spectra are asymmetric, where the first-order lower sideband $\omega - n\Delta\omega$ is always weaker than the upper sideband $\omega + n\Delta\omega$ for a n FSR comb ($n = 1, \dots, 5$). This actually implies that the sideband mode $\omega - n\Delta\omega$ is phase-matched (62), as the SF generation process, i.e., $(\omega - n\Delta\omega) + \omega \rightarrow 2\omega - n\Delta\omega$, also serves as an additional loss channel for the mode $\omega - n\Delta\omega$. It is worth mentioning that weak peaks located at the frequency $\omega - n\Delta\omega/2$ in between the pump and first-order lower sidebands are observed in the primary comb spectra. They are artifacts of the optical spectrum analyzer that records the second-order diffraction of the SF component $2\omega - n\Delta\omega$.

Moreover, we characterize the $\chi^{(2)}$ grating in the microresonator at each pump detuning denoted in Fig. 3 (A and B). The grating images measured at the conditions of SH and five-FSR comb generation are respectively shown in Fig. 2 (A and D), while the other grating images are displayed in note S4. It can be seen that, initially, there is only one grating (FH-SH grating), starting from SH generation up to two-FSR comb. Therefore, the SF-coupled primary comb generation process is supported by the same grating as for SH generation. The SH mode involved in the process is identified to be the fundamental transverse electric (TE) mode (SH1), whose FSR difference with the FH mode is the smallest among SH modes (see note S1). Given the distinct red-shift speeds of FH and SH resonances, such a small FSR difference allows for maximum comb FSR and SF mode switching ($n = 1, \dots, 5$) within the pump thermal triangle. The secondary grating (FH-SH-TH grating) appears from three to five FSR cases supporting the cascaded harmonic generation. The relative amplitude between the two gratings varies with pump detuning, as shown in note S4.

Figure 3 (C and D) shows the transmission and spectrum measurements for the 1547.35-nm pump resonance, for which we had recognized the SH mode involved in the SH and SF generation process as the second TE mode (SH2). As a consequence, the FSR difference between the SH and FH is larger compared to the previous 1544.40-nm resonance (see note S1), and less number of FSR switching events is expected to occur within the pump thermal triangle. Experimentally, we indeed obtain successive primary combs ($n = 1, 2, 3$) with comb spacing up to three FSR and SF component three FSR offset from the SH mode. Apart from the two resonances presented in Fig. 3, the FH-SH $\chi^{(2)}$ grating inscription and subsequent SF-coupled primary comb are found ubiquitous in many pumped resonances within C-band, owing to the high Q and small FSR of the microresonator used.

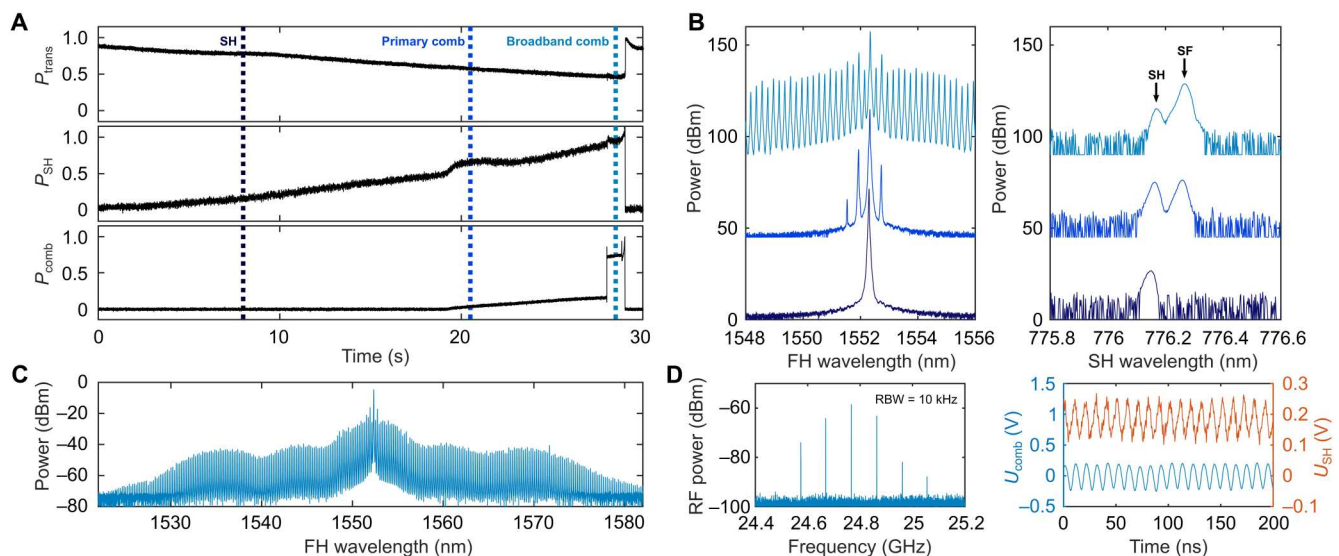


Fig. 4. Generation and characterization of the dark pulse microcomb. (A) Evolution of pump transmission (P_{trans}), generated SH power (P_{SH}), and comb power (P_{comb}) during the pump wavelength sweep across the resonance at 1552.34 nm. (B) The measured FH (left) and SH (right) spectra at the wavelength regions indicated by the vertical colored lines in (A). Initially, SH is generated, two-FSR primary comb is then followed with the simultaneous SF generation, and eventually evolves into a broadband dark pulse state. (C) The full spectrum of the generated dark pulse state. (D) Repetition-rate beat note (left) and time dynamics of comb and SH power (right) characterized at the dark pulse state. Multiple peaks spaced by 97.4 MHz are measured with 10-kHz resolution bandwidth (RBW), which matches the ~ 10 -ns oscillation periods of the comb and SH power. The measurements indicate that the spectrum in (C) corresponds to a dark pulse breather state.

Broadband microcomb generation

Besides the aforementioned switching primary combs, broadband microcombs can also be formed in the microresonator with the assistance of SF coupling, as shown in Fig. 4. Comb generation occurs for the 1552.34-nm resonance where gratings depicted in Fig. 2 (C and F) are inscribed. Figure 4A illustrates the transmission curves of the pump, SH, and comb power when sweeping across the resonance. Three characteristic states are identified in the transmission curves: only SH generation, two-FSR primary comb, and the broadband comb state, whose FH and SH spectra are presented in Fig. 4B (from bottom to top, respectively). Once the FH-SH grating is inscribed, it is noted that the two-FSR primary comb is first generated with clear SF coupling at the frequency $\omega - 2\Delta\omega$. We do not observe one-FSR comb in between the SH generation and two-FSR comb state. This may be linked to the initial relative resonance detuning condition at FH and SH bands—the nonlinear coupling is not strong enough to give rise to MI for the one-FSR sideband. Moreover, no FSR switching is cascaded during the pump sweep due to the large FSR mismatch between the FH and the participating SH mode (SH3). Instead, the primary comb evolves directly into a broadband microcomb, whose full spectrum is shown in Fig. 4C. A typical dark pulse comb shape in the normal dispersion regime is observed, covering the whole C-band with ~ 25 -GHz frequency grid. There are around 250 comb lines 10 dB above the noise floor of the optical spectrum analyzer, roughly corresponding to a comb span of 6 THz. It is worth mentioning that the dark pulse comb here emerges from the interlocked connection of switching waves (51) rather than the phase-matched $\chi^{(2)}$ process. However, the $\chi^{(2)}$ coupling-induced MI initiates the formation of primary combs or equivalently the Turing rolls (62). Such temporal patterns indeed facilitate the excitation of the dark pulse states (51), similar to other linear (55, 56) and nonlinear (49, 63) coupling approaches.

Thanks to the small FSR of the microresonator, we are able to characterize the beat note of the generated comb using a fast photodetector. From the measured radio-frequency (RF) spectrum in Fig. 4D, we observe multiple peaks equally spaced by 97.4 MHz with respect to the center frequency 24.77 GHz (the FSR at FH). The clear beat note signal indicates that the generated comb is a low-noise breather state (64, 65). Also, as shown in Fig. 4D, we measure the breathing dynamics of the generated comb power (pump filtered) and SH power. Because of the dispersion of the objective lens used, the measurements are done separately by adjusting the distance between the lens and the chip output; therefore, their relative oscillation phase is unknown. Nevertheless, it can be seen that the comb and SH power exhibit the same breathing period, ~ 10 ns, well matching the RF spectrum measurement. They are coupled via the SF generation process, where a large breathing depth at SH band is observed (mainly the SF component as indicated by the spectrum in Fig. 4D). Another interesting feature of the generated dark pulse state is that it can be accessed in a deterministic fashion (see note S5). The same comb state is reached with five consecutive pump sweeps, implying that the current comb excitation route does not undergo the chaotic region (66).

DISCUSSION

The nonlinear phenomena studied in this work result from the intrinsic $\chi^{(3)}$ and photo-induced $\chi^{(2)}$ nonlinearities in Si_3N_4 microresonators. Combined $\chi^{(2)}$ and $\chi^{(3)}$ nonlinear effects have been

demonstrated in other platforms, for example, in aluminum nitride microresonators (26, 52), exploiting intermodal phase matching for the $\chi^{(2)}$ process. In principle, these effects should also occur in microresonators with periodic $\chi^{(2)}$ domain inversion (12, 13). As opposed to the conventional electric field poling method, the photogalvanic effect recently observed in Si_3N_4 microresonators has significantly simplified the efforts required to write such QPM structures (40). Instead of being fixed, the photogalvanic $\chi^{(2)}$ gratings can be reconfigured at different pump resonances, thus offering much more possibility for exploiting $\chi^{(2)}$ and $\chi^{(3)}$ nonlinear interactions. In this study, we experimentally demonstrate several cascaded nonlinear effects: cascaded harmonic generation via the self-organized FH-SH-TH grating, consecutive switching of primary comb FSR and SF generation within one pump resonance, and the broad dark pulse comb generation.

In particular, the FH-SH-TH grating is appealing as it links three widely separated frequencies at visible, near visible, and telecom bands. The simultaneous SH and effective TH generation has also been previously achieved in $\chi^{(2)}$ crystals (60) and microcavities (67) by electric field poling, but their underlying domain structures contribute little to the FH-SH-TH grating components. By contrast, the photogalvanic effect self-organizes such a grating with the exactly desired periodicity. To fully exploit these distant spectral bands, a specially designed bus waveguide would be needed for efficient SH and TH light coupling. With regard to the FH-SH grating, despite being inscribed by the interference of pump and SH waves (photogalvanic SH generation process), it also automatically provides the phase-matching condition for the SF generation process. This effectively perturbs the phase of the corresponding sideband mode at FH and serves as an alternative approach for comb initiation in the normal dispersion regime. Since the photogalvanic effect in Si_3N_4 has also been demonstrated at 1- μm band (33), the method can be adapted toward shorter wavelength range where the dispersion is highly normal, dominated by the material dispersion of Si_3N_4 (49). The simultaneous SH and comb generation is of prominent interest for the self-referencing and the stabilization of the comb. In the current study, only the low-noise dark pulse breather comb is observed but not the stable state, which may be attributed to the high pump power and large detuning used in the experiment condition (54, 65), and further investigation is needed to better understand the generation of localized states in $\chi^{(3)}$ microresonators with photo-induced $\chi^{(2)}$ nonlinearity. At SH band, now, only the SH and SF modes are being prominently generated due to the FSR mismatch of the interacting FH and SH modes. Broadening the spectral bandwidth of the harmonic comb may be achieved in future work by proper waveguide engineering.

Owing to the slow time dynamics of the photogalvanic effect (39), all the pump wavelength sweeps conducted in the experiment are relatively slow, in the time scale of tens of seconds. Therefore, the cascaded nonlinear phenomena presented in this study can also be reliably reproduced by hand-tuning the laser frequency. While past works of $\chi^{(2)}$ and $\chi^{(3)}$ combs in Si_3N_4 microresonators have assumed intermodal phase matching for the $\chi^{(2)}$ process (48, 49), here, we unambiguously confirm the optical inscription of several QPM gratings and observe cascaded effects of different behaviors depending on the participating SH modes. This work displays the enormous potential of Si_3N_4 microresonators for the investigation and application of combined $\chi^{(2)}$ and $\chi^{(3)}$ nonlinear effects in a platform

that low loss and flexibility of optically induced $\chi^{(2)}$ phase matching can be exploited.

MATERIALS AND METHODS

Device information

The Si_3N_4 microresonator we used in the experiment is fabricated by the photonic Damascene process that features ultralow loss operation (68). It is a ring structure (radius $R = 924\ \mu\text{m}$) coupled with a bus waveguide, both buried in SiO_2 cladding and spaced 500 nm apart. The waveguide cross sections (width \times height) are around 2150 nm by 572 nm, which support multiple spatial modes at SH and TH wavelengths (see note S1). At FH wavelength, the intrinsic linewidths and coupling strengths of the fundamental TE mode resonances in the C-band are roughly 30 and 60 MHz, respectively (see note S1). Besides, the microresonator is characterized to exhibit normal dispersion at pump wavelength.

TPM imaging and processing

For characterization of the inscribed $\chi^{(2)}$ gratings, a high-power femtosecond Ti:sapphire laser is focused at the grating plane of the microresonator in an upright configuration. The focal spot is then raster-scanned across the plane, while, in the meantime, its generated SH signal is monitored so that the $\chi^{(2)}$ response is probed. After TPM images are obtained, we project the circular arc of the microresonator into a straight line so as to facilitate further processing (40). Specifically, we set the microresonator's center as the origin and map the point ($\rho\cos\phi$, $\rho\sin\phi$) in the measured image (ρ the distance and ϕ the polar angle with respect to the center of the microresonator) to the point (ρ , $\rho\phi$) in the new image. Since the grating is written in the microresonator around $\rho = R$, we define $l = \rho\phi$ and $r = \rho - R$ in Fig. 1 for clarity.

Supplementary Materials

This PDF file includes:

Supplementary Text
Figs. S1 to S5

REFERENCES AND NOTES

1. I. Breunig, Three-wave mixing in whispering gallery resonators. *Laser Photonics Rev.* **10**, 569–587 (2016).
2. D. J. Moss, R. Morandotti, A. L. Gaeta, M. Lipson, New CMOS-compatible platforms based on silicon nitride and hydex for nonlinear optics. *Nat. Photonics* **7**, 597–607 (2013).
3. S. M. Spillane, T. J. Kippenberg, K. J. Vahala, Ultralow-threshold raman laser using a spherical dielectric microcavity. *Nature* **415**, 621–623 (2002).
4. B. J. Eggleton, C. G. Poulton, P. T. Rakich, M. J. Steel, G. Bahl, Brillouin integrated photonics. *Nat. Photonics* **13**, 664–677 (2019).
5. J. B. Surya, X. Guo, C.-L. Zou, H. X. Tang, Efficient third-harmonic generation in composite aluminum nitride/silicon nitride microrings. *Optica* **5**, 103–108 (2018).
6. A. Pasquazi, M. Peccianti, L. Razzari, D. J. Moss, S. Coen, M. Erkintalo, Y. K. Chembo, T. Hansson, S. Wabnitz, P. Del'Haye, X. Xue, A. M. Weiner, R. Morandotti, Micro-combs: A novel generation of optical sources. *Phys. Rep.* **729**, 1–81 (2018).
7. T. Kippenberg, S. Spillane, K. Vahala, Kerr-nonlinear optical parametric oscillation in an ultrahigh-Q toroid microcavity. *Phys. Rev. Lett.* **93**, 083904 (2004).
8. T. Herr, V. Brasch, J. D. Jost, C. Y. Wang, N. M. Kondratiev, M. L. Gorodetsky, T. J. Kippenberg, Temporal solitons in optical microresonators. *Nat. Photonics* **8**, 145–152 (2014).
9. X. Xue, Y. Xuan, Y. Liu, P.-H. Wang, S. Chen, J. Wang, D. E. Leaird, M. Qi, A. M. Weiner, Mode-locked dark pulse Kerr combs in normal-dispersion microresonators. *Nat. Photonics* **9**, 594–600 (2015).
10. T. J. Kippenberg, A. L. Gaeta, M. Lipson, M. L. Gorodetsky, Dissipative Kerr solitons in optical microresonators. *Science* **361**, eaan8083 (2018).
11. J. Lin, N. Yao, Z. Hao, J. Zhang, W. Mao, M. Wang, W. Chu, R. Wu, Z. Fang, L. Qiao, W. Fang, F. Bo, Y. Cheng, Broadband quasi-phase-matched harmonic generation in an on-chip monocrystalline lithium niobate microdisk resonator. *Phys. Rev. Lett.* **122**, 173903 (2019).
12. J.-Y. Chen, Z.-H. Ma, Y. M. Sua, Z. Li, C. Tang, Y.-P. Huang, Ultra-efficient frequency conversion in quasi-phase-matched lithium niobate microrings. *Optica* **6**, 1244–1245 (2019).
13. J. Lu, M. Li, C.-L. Zou, A. Al Sayem, H. X. Tang, Toward 1% single-photon anharmonicity with periodically poled lithium niobate microring resonators. *Optica* **7**, 1654–1659 (2020).
14. A. W. Bruch, X. Liu, X. Guo, J. B. Surya, Z. Gong, L. Zhang, J. Wang, J. Yan, H. X. Tang, 17 000%/w second-harmonic conversion efficiency in single-crystalline aluminum nitride microresonators. *Appl. Phys. Lett.* **113**, 131102 (2018).
15. P. S. Kuo, J. Bravo-Abad, G. S. Solomon, Second-harmonic generation using-quasi-phase-matching in a GaAs whispering-gallery-mode microcavity. *Nat. Commun.* **5**, 1–7 (2014).
16. A. D. Logan, M. Gould, E. R. Schmidgall, K. Hestroffer, Z. Lin, W. Jin, A. Majumdar, F. Hatami, A. W. Rodriguez, K.-M. C. Fu, 400%/w second harmonic conversion efficiency in 14 μm -diameter gallium phosphide-on-oxide resonators. *Opt. Express* **26**, 33687–33699 (2018).
17. J. Szabados, D. N. Puzyrev, Y. Minet, L. Reis, K. Buse, A. Villosio, D. V. Skryabin, I. Breunig, Frequency comb generation via cascaded second-order nonlinearities in microresonators. *Phys. Rev. Lett.* **124**, 203902 (2020).
18. I. Hendry, L. S. Trainor, Y. Xu, S. Coen, S. G. Murdoch, H. G. Schwefel, M. Erkintalo, Experimental observation of internally pumped parametric oscillation and quadratic comb generation in a $\chi^{(2)}$ whispering-gallery-mode microresonator. *Opt. Lett.* **45**, 1204–1207 (2020).
19. I. Ricciardi, S. Mosca, M. Parisi, P. Maddaloni, L. Santamaria, P. De Natale, M. De Rosa, Frequency comb generation in quadratic nonlinear media. *Phys. Rev. A* **91**, 063839 (2015).
20. S. Mosca, I. Ricciardi, M. Parisi, P. Maddaloni, L. Santamaria, P. De Natale, M. De Rosa, Direct generation of optical frequency combs in $\chi^{(2)}$ nonlinear cavities. *Nanophotonics* **5**, 316–331 (2016).
21. F. Leo, T. Hansson, I. Ricciardi, M. De Rosa, S. Coen, S. Wabnitz, M. Erkintalo, Walk-off-induced modulation instability, temporal pattern formation, and frequency comb generation in cavity-enhanced second-harmonic generation. *Phys. Rev. Lett.* **116**, 033901 (2016).
22. T. Beckmann, H. Linnenbank, H. Steigerwald, B. Sturman, D. Haertle, K. Buse, I. Breunig, Highly tunable low-threshold optical parametric oscillation in radially poled whispering gallery resonators. *Phys. Rev. Lett.* **106**, 143903 (2011).
23. A. W. Bruch, X. Liu, J. B. Surya, C.-L. Zou, H. X. Tang, On-chip $\chi^{(2)}$ microring optical parametric oscillator. *Optica* **6**, 1361–1366 (2019).
24. J. Szabados, B. Sturman, I. Breunig, Frequency comb generation threshold via second-harmonic excitation in $\chi^{(2)}$ optical microresonators. *APL Photonics* **5**, 116102 (2020).
25. J. Lu, A. Al Sayem, Z. Gong, J. B. Surya, C.-L. Zou, H. X. Tang, Ultralow-threshold thin-film lithium niobate optical parametric oscillator. *Optica* **8**, 539–544 (2021).
26. A. W. Bruch, X. Liu, Z. Gong, J. B. Surya, M. Li, C.-L. Zou, H. X. Tang, Pockels soliton microcomb. *Nat. Photonics* **15**, 21–27 (2021).
27. D. M. Lukin, C. Dory, M. A. Guidry, K. Y. Yang, S. D. Mishra, R. Trivedi, M. Radulaski, S. Sun, D. Vercruysse, G. H. Ahn, J. Vučković, 4H-silicon-carbide-on-insulator for integrated quantum and nonlinear photonics. *Nat. Photonics* **14**, 330–334 (2020).
28. C. Wang, Z. Fang, A. Yi, B. Yang, Z. Wang, L. Zhou, C. Shen, Y. Zhu, Y. Zhou, R. Bao, Z. Li, Y. Chen, K. Huang, J. Zhang, Y. Cheng, X. Ou, High-Q microresonators on 4H-silicon-carbide-on-insulator platform for nonlinear photonics. *Light Sci. Appl.* **10**, 1–11 (2021).
29. E. Timurdogan, C. V. Poulton, M. Byrd, M. Watts, Electric field-induced second-order nonlinear optical effects in silicon waveguides. *Nat. Photonics* **11**, 200–206 (2017).
30. N. Singh, M. Raval, A. Ruocco, M. R. Watts, Broadband 200-nm second-harmonic generation in silicon in the telecom band. *Light Sci. Appl.* **9**, 17 (2020).
31. C. Castellano, A. Trenti, C. Vecchi, A. Marchesini, M. Mancinelli, M. Ghulinyan, G. Pucker, L. Pavesi, On the origin of second harmonic generation in silicon waveguides with silicon nitride cladding. *Sci. Rep.* **9**, 1–12 (2019).
32. A. Billat, D. Grassani, M. H. Pfeiffer, S. Kharitonov, T. J. Kippenberg, C.-S. Brès, Large second harmonic generation enhancement in Si_3N_4 waveguides by all-optically induced quasi-phase-matching. *Nat. Commun.* **8**, 1–7 (2017).
33. M. A. Porcel, J. Mak, C. Taballione, V. K. Schermerhorn, J. P. Epping, P. J. van der Slot, K.-J. Boller, Photo-induced second-order nonlinearity in stoichiometric silicon nitride waveguides. *Opt. Express* **25**, 33143–33159 (2017).
34. D. D. Hickstein, D. R. Carlson, H. Munday, J. B. Khurgin, K. Srinivasan, D. Westly, A. Kowligy, I. I. Smalyukh, S. A. Diddams, S. B. Papp, Self-organized nonlinear gratings for ultrafast nanophotonics. *Nat. Photonics* **13**, 494–499 (2019).
35. E. Nitiss, T. Liu, D. Grassani, M. Pfeiffer, T. J. Kippenberg, C.-S. Brès, Formation rules and dynamics of photoinduced $\chi^{(2)}$ gratings in silicon nitride waveguides. *ACS Photonics* **7**, 147–153 (2019).

36. O. Yakar, E. Nitiss, J. Hu, C.-S. Brès, Generalized coherent photogalvanic effect in coherently seeded waveguides. *Laser Photonics Rev.*, 2200294 (2022).
37. X. Zhang, Q.-T. Cao, Z. Wang, Y.-X. Liu, C.-W. Qiu, L. Yang, Q. Gong, Y.-F. Xiao, Symmetry-breaking-induced nonlinear optics at a microcavity surface. *Nat. Photonics* **13**, 21–24 (2019).
38. J. S. Levy, M. A. Foster, A. L. Gaeta, M. Lipson, Harmonic generation in silicon nitride ring resonators. *Opt. Express* **19**, 11415–11421 (2011).
39. X. Lu, G. Moille, A. Rao, D. A. Westly, K. Srinivasan, Efficient photoinduced second-harmonic generation in silicon nitride photonics. *Nat. Photonics* **15**, 131–136 (2021).
40. E. Nitiss, J. Hu, A. Stroganov, C.-S. Brès, Optically reconfigurable quasi-phase-matching in silicon nitride microresonators. *Nat. Photonics* **16**, 1–8 (2022).
41. D. Z. Anderson, V. Mizrahi, J. E. Sipe, Model for second-harmonic generation in glass optical fibers based on asymmetric photoelectron emission from defect sites. *Opt. Lett.* **16**, 796–798 (1991).
42. E. M. Dianov, D. S. Starodubov, Photoinduced generation of the second harmonic in centrosymmetric media. *Quantum Electron.* **25**, 395–407 (1995).
43. W. Margulis, F. Laurell, B. Lesche, Imaging the nonlinear grating in frequency-doubling fibres. *Nature* **378**, 699–701 (1995).
44. F. Ferdous, H. Miao, D. E. Leaird, K. Srinivasan, J. Wang, L. Chen, L. T. Varghese, A. M. Weiner, Spectral line-by-line pulse shaping of on-chip microresonator frequency combs. *Nat. Photonics* **5**, 770–776 (2011).
45. V. Brasch, M. Geiselmann, T. Herr, G. Lihachev, M. H. Pfeiffer, M. L. Gorodetsky, T. J. Kippenberg, Photonic chip-based optical frequency comb using soliton Cherenkov radiation. *Science* **351**, 357–360 (2016).
46. B. Stern, X. Ji, Y. Okawachi, A. L. Gaeta, M. Lipson, Battery-operated integrated frequency comb generator. *Nature* **562**, 401–405 (2018).
47. C. Xiang, J. Liu, J. Guo, L. Chang, R. N. Wang, W. Weng, J. Peters, W. Xie, Z. Zhang, J. Riemensberger, J. Selvidge, T. J. Kippenberg, J. E. Bowers, Laser soliton microcombs heterogeneously integrated on silicon. *Science* **373**, 99–103 (2021).
48. S. Miller, K. Luke, Y. Okawachi, J. Cardenas, A. L. Gaeta, M. Lipson, On-chip frequency comb generation at visible wavelengths via simultaneous second-and third-order optical nonlinearities. *Opt. Express* **22**, 26517–26525 (2014).
49. X. Xue, F. Leo, Y. Xuan, J. A. Jaramillo-Villegas, P.-H. Wang, D. E. Leaird, M. Erkintalo, M. Qi, A. M. Weiner, Second-harmonic-assisted four-wave mixing in chip-based microresonator frequency comb generation. *Light Sci. Appl.* **6**, e16253 (2017).
50. W. Seka, S. Jacobs, J. Rizzo, R. Boni, R. Craxton, Demonstration of high efficiency third harmonic conversion of high power Nd-glass laser radiation. *Opt. Commun.* **34**, 469–473 (1980).
51. P. Parra-Rivas, D. Gomila, E. Knobloch, S. Coen, L. Gelens, Origin and stability of dark pulse Kerr combs in normal dispersion resonators. *Opt. Lett.* **41**, 2402–2405 (2016).
52. H. Jung, R. Stoll, X. Guo, D. Fischer, H. X. Tang, Green, red, and IR frequency comb line generation from single IR pump in AlN microring resonator. *Optica* **1**, 396–399 (2014).
53. Y. He, Q.-F. Yang, J. Ling, R. Luo, H. Liang, M. Li, B. Shen, H. Wang, K. Vahala, Q. Lin, Self-starting bi-chromatic LiNbO₃ soliton microcomb. *Optica* **6**, 1138–1144 (2019).
54. C. Godey, I. V. Balakireva, A. Coillet, Y. K. Chembo, Stability analysis of the spatiotemporal lugiato-lefever model for Kerr optical frequency combs in the anomalous and normal dispersion regimes. *Phys. Rev. A* **89**, 063814 (2014).
55. Y. Liu, Y. Xuan, X. Xue, P.-H. Wang, S. Chen, A. J. Metcalf, J. Wang, D. E. Leaird, M. Qi, A. M. Weiner, Investigation of mode coupling in normal-dispersion silicon nitride microresonators for Kerr frequency comb generation. *Optica* **1**, 137–144 (2014).
56. X. Xue, Y. Xuan, P.-H. Wang, Y. Liu, D. E. Leaird, M. Qi, A. M. Weiner, Normal-dispersion microcombs enabled by controllable mode interactions. *Laser Photonics Rev.* **9**, L23–L28 (2015).
57. G. Lihachev, W. Weng, J. Liu, L. Chang, J. Guo, J. He, R. N. Wang, M. H. Anderson, Y. Liu, J. E. Bowers, T. J. Kippenberg, Platicon microcomb generation using laser self-injection locking. *Nat. Commun.* **13**, 1–9 (2022).
58. F. Leo, T. Hansson, I. Ricciardi, M. De Rosa, S. Coen, S. Wabnitz, M. Erkintalo, Frequency-comb formation in doubly resonant second-harmonic generation. *Phys. Rev. A* **93**, 043831 (2016).
59. L. Wang, L. Chang, N. Volet, M. H. Pfeiffer, M. Zervas, H. Guo, T. J. Kippenberg, J. E. Bowers, Frequency comb generation in the green using silicon nitride microresonators. *Laser Photonics Rev.* **10**, 631–638 (2016).
60. S.-N. Zhu, Y.-Y. Zhu, N.-B. Ming, Quasi-phase-matched third-harmonic generation in a quasi-periodic optical superlattice. *Science* **278**, 843–846 (1997).
61. K. Sasagawa, M. Tsuchiya, Highly efficient third harmonic generation in a periodically poled MgO:LiNbO₃ disk resonator. *Appl. Phys. Express* **2**, 122401 (2009).
62. S.-W. Huang, J. Yang, S.-H. Yang, M. Yu, D.-L. Kwong, T. Zelevinsky, M. Jarrahi, C. W. Wong, Globally stable microresonator Turing pattern formation for coherent high-power THz radiation on-chip. *Phys. Rev. X* **7**, 041002 (2017).
63. A. Cherenkov, N. Kondratiev, V. Lobanov, A. Shitikov, D. Skryabin, M. Gorodetsky, Raman-Kerr frequency combs in microresonators with normal dispersion. *Opt. Express* **25**, 31148–31158 (2017).
64. E. Lucas, M. Karpov, H. Guo, M. Gorodetsky, T. J. Kippenberg, Breathing dissipative solitons in optical microresonators. *Nat. Commun.* **8**, 1–11 (2017).
65. C. Bao, Y. Xuan, C. Wang, A. Fülöp, D. E. Leaird, V. Torres-Company, M. Qi, A. M. Weiner, Observation of breathing dark pulses in normal dispersion optical microresonators. *Phys. Rev. Lett.* **121**, 257401 (2018).
66. E. Nazemosadat, A. Fülöp, Ö. B. Helgason, P.-H. Wang, Y. Xuan, D. E. Leaird, M. Qi, E. Silvestre, A. M. Weiner, V. Torres-Company, Switching dynamics of dark-pulse Kerr frequency comb states in optical microresonators. *Phys. Rev. A* **103**, 013513 (2021).
67. L. Zhang, Z. Hao, Q. Luo, A. Gao, R. Zhang, C. Yang, F. Gao, F. Bo, G. Zhang, J. Xu, Dual-periodically poled lithium niobate microcavities supporting multiple coupled parametric processes. *Opt. Lett.* **45**, 3353–3356 (2020).
68. J. Liu, G. Huang, R. N. Wang, J. He, A. S. Raja, T. Liu, N. J. Engelsens, T. J. Kippenberg, High-yield, wafer-scale fabrication of ultralow-loss, dispersion-engineered silicon nitride photonic circuits. *Nat. Commun.* **12**, 1–9 (2021).

Acknowledgments

Funding: This work was supported by ERC grant PISSARRO (ERC-2017-CoG 771647), by the Air Force Office of Scientific Research (AFOSR) under award no. FA9550-19-1-0250, by contract HR0011-20-2-0046 (NOVEL) from the Defense Advanced Research Projects Agency (DARPA), Microsystems Technology Office (MTO), and by the Swiss National Science Foundation under grant agreement no. 176563 (BRIDGE). **Author contributions:** J. Hu, E.N., and J. He led the experiment, carried out the measurements, and analyzed the data. J. Hu, E.N., and O.Y. explained the cascaded effects and performed the theoretical analysis and numerical simulation with assistance from J. He and W.W. J.L. and J. He fabricated and characterized the device. T.J.K. supervised the device fabrication and comb generation. J. Hu, E.N., and C.-S.B. wrote the manuscript with input from all authors. C.-S.B. supervised the project. **Competing interests:** The authors declare that they have no competing interests. **Data and materials availability:** All data needed to evaluate the conclusions in the paper are present in the paper and/or the Supplementary Materials. The data and code used to produce the results of this manuscript are available on Zenodo: <https://doi.org/10.5281/zenodo.7266982>.

Submitted 6 July 2022

Accepted 8 November 2022

Published 14 December 2022

10.1126/sciadv.add8252